Calculating structural and geometrical parameters by laboratory measurements and X-ray microtomography: a comparative study applied to a limestone sample before and after a dissolution experiment

Linda Luquot, Vanessa Hebert, Olivier Rodriguez

Solid Earth, 7, 441–456, 2016
www.solid-earth.net/7/441/2016/
doi:10.5194/se-7-441-2016

Solid Earth Open Access EGU

Calculating structural and geometrical parameters by laboratory measurements and X-ray microtomography: a comparative study applied to a limestone sample before and after a dissolution experiment

Linda Luquot[1], Vanessa Hebert[2], and Olivier Rodriguez[2]

[1]Institute of Environmental Assessment and Water Research (IDAEA), Hydrogeology Group (UPC-CSIC), c/ Jordi Girona 18, 08034 Barcelona, Spain
[2]Voxaya SAS, Cap Omega, Rond-Point Benjamin Franklin, CS 39521, 34960 Montpellier, France

Correspondence to: Linda Luquot (linda.luquot@idaea.csic.es)

Received: 30 October 2015 – Published in Solid Earth Discuss.: 26 November 2015
Revised: 4 February 2016 – Accepted: 9 March 2016 – Published: 24 March 2016

Abstract. The aim of this study is to compare the structural, geometrical and transport parameters of a limestone rock sample determined by X-ray microtomography (XMT) images and laboratory experiments. Total and effective porosity, pore-size distribution, tortuosity, and effective diffusion coefficient have been estimated. Sensitivity analyses of the segmentation parameters have been performed. The limestone rock sample studied here has been characterized using both approaches before and after a reactive percolation experiment. Strong dissolution process occurred during the percolation, promoting a wormhole formation. This strong heterogeneity formed after the percolation step allows us to apply our methodology to two different samples and enhance the use of experimental techniques or XMT images depending on the rock heterogeneity. We established that for most of the parameters calculated here, the values obtained by computing XMT images are in agreement with the classical laboratory measurements. We demonstrated that the computational porosity is more informative than the laboratory measurement. We observed that pore-size distributions obtained by XMT images and laboratory experiments are slightly different but complementary. Regarding the effective diffusion coefficient, we concluded that both approaches are valuable and give similar results. Nevertheless, we concluded that computing XMT images to determine transport, geometrical, and petrophysical parameters provide similar results to those measured at the laboratory but with much shorter durations.

1 Introduction

Characterizing the rock pore structure such as the porosity, the total pore–rock interface and the connectivity is essential to evaluate oil or gas production or volume of stored CO_2 in case of geological sequestration, for example. Porosity is a key petrophysical parameter, indicating the total volume of oil, gas, or water that can be contained in a reservoir. It is essential to differentiate the total porosity from the open connected or effective porosity, which is the fraction of porosity accessible by any fluid. Connectivity as well as permeability and tortuosity allow us to quantify the ability to extract or inject fluids. The higher the connectivity and permeability are and the lower the tortuosity is, the higher the extraction or injection flow rate will be. In consolidated rock aquifers, the groundwater flow occurs through discrete openings, i.e. fractures, and only to a small extent in the pore-network of the rock matrix. The migration of solutes and solvents in fractured rock aquifers is therefore determined by the relative contribution of advective flow compared to matrix diffusion transverse to the flow direction, resulting in the retardation of the solute. The advection transport is controlled by the permeability of the reservoir (mainly controlled by fracture or preferential flow path as wormhole or karst conduit), whereas the diffusion through the matrix depends of the effective diffusion coefficient, which is linked to tortuosity, effective porosity and cementation factor (Archie, 1942; Fick, 1855). Diffusion in rock, of either gas or liquid phase, could

be the rate-limiting or dominant process in many scenarios, such as geologic disposal of radioactive waste (Gillham et al., 1984), contaminant remediation (e.g., Becker and Shapiro, 2003), CO_2 geological storage (Hatiboglu and Babadagli, 2010), and oil and gas recovery (Cui et al., 2004, 2009). Diffusion of hazardous gas or liquid chemicals in construction materials has also become a concern for public health and security (Nestle et al., 2001a, b). Therefore, knowledge of diffusion processes and rates in rocks is important to better understand these issues.

To evaluate all these parameters, different laboratory petrophysical techniques are usually used. Some of them are time consuming and destructive methods, such as mercury pore-size measurement or BET (Brunauer–Emmett–Teller) surface analysis. Moreover, these different techniques are performed at different sample scales and may require prior preparation, such as thin section for SEM (Scanning Electron Microscope) analysis, for example. Yet, most of the laboratories techniques used and discussed in this article are fully validated.

Currently, a lot of petrophysical, geometrical, transport and mechanical parameters are computed using 3-D X-ray microtomography (XMT) images (Alshibli and Reed, 2012). High resolution 3-D XMT is a powerful technique used to image and characterize the internal structure and geometry of natural and/or artificial objects. It is a non-destructive method that does not need prior sample treatment, such as impregnation, thinning or polishing (Remeysen and Swennen, 2008). In this technique, contiguous sequential images are compiled to create 3-D representations that may be digitally processed to obtain relevant quantitative geometric and/or morphological parameters (Ketcham and Carlson, 2001). 3-D data provides access to some very important geometric and topological characteristics such as size, shape, orientation distribution of individual features and that of their local neighbourhoods, connectivity between features and network, composition, etc. Computational techniques have progressed to the point where material properties such as conductivity (Arns et al., 2001), diffusivity (Schwartz et al., 1994; Knackstedt et al., 2006; Promentilla et al., 2009; Gouze and Luquot, 2011), permeability (Martys et al., 1999; Arns et al., 2004; Arns et al., 2005a; Arns et al., 2005b), pore-size distribution (Dunsmuir et al., 1991; Prodanovic et al., 2010; Garing et al., 2014; Luquot et al., 2014a) and linear elasticity (Roberts and Garboczi, 2000; Arns et al., 2002; Knackstedt et al., 2006) can be calculated on large three-dimensional digitized grids (over 10^9 voxels). More details on this technique, acquisition and data computing step can be found in Taina et al. (2008); Cnudde and Boone (2013) and Wildenschild and Sheppard (2013). In geosciences, the internal structure of a great diversity of geological samples has been examined by radiographic imaging mainly in the last 50 years (Calvert and Veevers, 1962; Hamblin, 1962; Baker and Friedman, 1969; Herm, 1973; Sturmer, 1973; Bjerreskov, 1978; Monna et al., 1997; Louis et al., 2007; Schmidt et al., 2007).

Yet, to our knowledge, no study has been conducted to explore the potential links that can be made between variables computed from XMT images and those traditionally measured in the laboratory for a limestone core rock sample, before and after a dissolution process. Only one similar study was done by Lamande et al. (2013) on soil material using a medical scanner with a large pixel size (0.6 mm). Nevertheless, op. cited authors focused their study to only a few parameters.

Here, we use high resolution X-ray microtomography images to characterize the structural and geometrical parameters of a limestone core rock sample percolated by an acidic solution. We computed and experimentally measured, total and effective porosity, pore-size diameter distribution, effective diffusion coefficient, and tortuosity. These parameters are those needed for numerical modelling to evaluate oil and gas deposit volume and extraction flow rate, for example. Quantifying the pore network characteristics of a same sample before and after a dissolution experiment allows to apply our methodology to two different pore networks and enhance the use of experimental techniques or XMT images depending on the rock heterogeneity. The focus of the present study is to articulate the potential of variables estimated using XMT images and how these estimates compare with, and complement, traditional laboratory-based measurements.

2 Materials and methods

In this section, we describe the different laboratory measurements and XMT images computations to evaluate the various petrophysical, geometrical and hydrodynamic parameters. The list of these parameters and the corresponding methods are summarized in Table 1.

2.1 Laboratory methodology

2.1.1 Rock sample

The rock sample used in this study is an oolitic limestone almost composed of calcite ($CaCO_3$) and is named Bvl in the paper. This limestone is commonly referred to as Beauval rock and is coming from Beaunotte in Dordogne region in France. It is characterized by a beige colour with some shells. The mean connected porosity is usually comprised between 9 and 13 %, according to general information provided by quarry mining companies. The core sample diameter and length are respectively 2.5 and 2 cm.

2.1.2 Laboratory petrophysical characterization

In order to characterize the different geometrical and structural properties of the rock sample before and after the percolation experiments, we used different classical laboratory ex-

Table 1. Summary of the measured parameters and the corresponding methodologies. (seg.: segmentation, Psd: pore-size distribution, Msd: mean square diplacement, TPP: total porous phase, RPP: resolved porous phase, CRPP: connected resolved porous phase).

Analyzed properties		Methods of analysis		
		Lab measurement	XMT computing	
			XMT tools	Analyzed phases
Porosity	total volume fraction	–	Voxaya seg. algorithm	TPP
	calculation errors	–	Voxaya seg. algorithm	RPP
	effective porosity	triple weighing method	clustering algorithm	TPP
Geometric parameters	interface surface area	BET	Voxaya algorithm	CRPP
	Pore size	retention curves	Psd function and Euclidean distance	RPP
			chord-length algorithm	RPP
			Voxaya skeleton algorithm	CRPP
Hydrodynamic parameters	diffusion coefficient/tortuosity	through-diffusion experiment	Msd of virtual particles (Brownian motion)	CRPP
	permeability	pressure drop	–	–

periments. These different techniques have been performed following a home-methodology to avoid too many drying and wetting sample steps.

First of all, to evaluate the effective (connected) porosity, we used the triple weighing method. We first measured the dry sample weight after leaving the sample during 48 h in an oven at 40 °C. We then saturated the sample, starting by a sample vacuum step. Afterwards, we left the calcite equilibrated water penetrate into the pore structure and we weighed the saturated and submerged sample weights. We weighed four times the sample during the dry, saturated and submerged steps. This classical method is very time consuming and requires 4 entire days.

Then, we took advantage of the saturated sample state to evaluate the pore-size distribution by measuring the retention curve of the sample using a centrifuge and applying various rotation rates as previously done by Luquot et al. (2014b) and Roetting et al. (2015). The technique consists in applying a high gravity field to an initially saturated sample and measuring the drained volume of water. For this purpose, we used a Rotina® 420R centrifuge following the methodology of Reatto et al. (2008) using six speed increments up to 4500 rpm. The maximum suction that can be applied to the sample at 4500 rpm is 213 kPa. This technique allows us to measure the effective capillary size distribution and the retention curve $\theta(P)$, where θ is the volumetric water content and P is the capillary pressure (minus suction). By capillarity theory (Young-Laplace equation with cylindrical approximation), the minimum radius of a pore that drains at P is given by:

$$r_{\mathrm{p}} = \frac{-2\sigma\cos\alpha}{P}, \tag{1}$$

where σ is the surface tension ($72.3 \pm 0.5\,\mathrm{mN\,m^{-1}}$, Adamson and Gast, 1997) and α is the contact angle ($40 \pm 8°$, Espinoza and Santamarina, 2010). Using Eq. (1), we can convert the measured $\theta(P)$ into an equivalent $\theta(r_{\mathrm{p}})$ curve. This curve is actually a cumulative pore-size distribution; the water content $\theta(r_{\mathrm{p}})$ indicates the combined volume of all pores with opening radius less than r_{p}. The measurements were performed twice in the two directions to evaluate the sample anisotropy. Six days were necessary to acquire the retention curves in both directions two times, dry, and re-saturate the sample for the second measurement.

After the centrifuge step, we dried the sample again in an oven during 48 h at 40° and measured again the dry sample weight. We then repeated the triple weighing method to evaluate the initial porosity and took advantage of the saturation state of the sample to perform through-diffusion experiment. Classically, the effective diffusion coefficient as well as the tortuosity factor is measured by liquid phase conservative tracer test (usually iodine) as presented by Boving and Grathwohl (2001) and Luquot et al. (2014a).

Through-diffusion experiments were performed to determine the effective diffusion coefficient and tortuosity/constrictivity ratio before and after the dissolution experiment (Li and Gregory, 1974). The same methodology as the one developed by Luquot et al. (2014b) has been used here. The diffusion cell apparatus consisted of two acryl-glass cells of equal size and volume. The reservoir cell contained a $0.02\,\mathrm{mol\,L^{-1}}$ of potassium iodide tracer solution, whereas the sink cell did not contain any tracer at the beginning. We used Beauval rock equilibrated water in both reservoirs and we added several milligrams of sodium azide (NaN_3) to prevent biofilm formation. The mounted rock sample was sandwiched between the sink and reservoir cell. During the experiment, iodide ions diffuse from the reservoir cell into the sink cell through sample Bvl. An iodide-specific electrode from Cole–Parmer Instrument CO was used to measure the iodide concentration in the sink cell. More details about the procedure can be found in Luquot et al. (2014b). The aqueous diffusion coefficient for iodide ($D_{\mathrm{aq}} = 1.86 \times 10^{-9}\,\mathrm{m^2\,s^{-1}}$) (Robinson and Stokes, 1959) was used to calculate the effective diffusion coefficient D_{eff}. The effective diffusion coefficient was calculated using the equation (van Brakel and Heertjes, 1974; Crank, 1975):

$$D_{\mathrm{eff}} = \frac{\beta l}{C_0}, \tag{2}$$

where β is the slope of solute mass vs. time, which is obtained from linear regression of data in the steady-state range, l is the rock sample thickness and C_0 is the concentration in the reservoir cell. Then, it is possible to determine the tortuosity coefficient using the definition of the effective diffusion coefficient in a porous water-saturated media proposed by van Brakel and Heertjes (1974):

$$D_{\mathrm{eff}} = \frac{D_{\mathrm{aq}}\phi\delta}{\tau^2}, \tag{3}$$

where τ is tortuosity and δ is constrictivity. These coefficients are sometimes gathered together into an empirical exponent m, denoted cementation factor, as in the following equation:

$$D_{\mathrm{eff}} = D_{\mathrm{aq}}\phi^m \tag{4}$$

Through-diffusion experiment are time consuming because of the slow diffusion rate of a liquid tracer, even for porous limestone and sandstone samples (Boving and Grathwohl, 2001). One to two weeks are needed for each measurement.

2.1.3 Laboratory percolation experiment

We performed the flow-through experiment using the apparatus presented in Luquot et al. (2014b). The setup allows to inject at constant flow rate up to four different solutions in parallel through four distinct core samples. Various pressure sensors and a differential pressure sensor enable to monitor the inlet and outlet pressures and then calculate the sample permeability using Darcy's law. We injected an acidic solution through sample Bvl at constant flow rate $Q = 16\,\mathrm{mL\,h^{-1}}$ during 9 h at room temperature and pressure. The injected solution was an acetic acid at pH = 3.5 and buffered at 500 mM. We prepared the injected solution by mixing $28.43\,\mathrm{g\,L^{-1}}$ of acetic acid with 2.184 of sodium acetate. During the dissolution experiment, we continuously recorded the inlet and outlet pH and the pressure drop between the inlet and outlet of the sample to calculate the sample permeability. The total injected fluid was $146\,\mathrm{cm^3}$, or some 90 pore volumes of sample Bvl (initial pore volume $= 1.62\,\mathrm{cm^3}$).

Outlet water was sampled periodically, acidified to prevent mineral precipitation, and analyzed for concentrations of Ca using inductively coupled plasma-atomic emission spectrophotometry (ICP-AES, IDAEA, Spain). Reaction progress and porosity changes are calculated from the difference between injected and percolated waters, knowing that calcite is the only mineral composing the sample. Calcite dissolution is described as follows:

$$\mathrm{CaCO_3 + H^+ \rightleftharpoons Ca^{2+} + HCO_3^-}.. \tag{R1}$$

The volume of dissolved calcite ($\Delta V_{\mathrm{calcite}}(t)$) is calculated as follows:

$$\Delta V_{\mathrm{calcite}}(t) = \upsilon Q \int_{t'=0}^{t'=t} \Delta C_{\mathrm{Ca}}(t')\mathrm{d}t', \tag{5}$$

where υ is the calcite molar volume ($3.7 \times 10^{-5}\,\mathrm{m^3\,mol^{-1}}$), and ΔC_{Ca} is the difference between the outlet and inlet calcium concentration. Therefore, we can calculate the sample-scale porosity change during the percolation experiment using the following equation:

$$\phi(t) = \phi_0 + \frac{\Delta V_{\mathrm{calcite}}(t)}{V}, \tag{6}$$

where V is the total sample volume and ϕ_0 is the initial sample porosity. The error $\epsilon(\Delta C_{\mathrm{Ca}})$ in the change of calcium concentration was estimated using the Gaussian error propagation method (Barrante, 1974). The calculated error is propagated to the porosity estimation. After the percolation experiment, we characterized the core rock sample using the same methodology as before, described in Sect. 2.1.2.

2.2 X-ray microtomography images

2.2.1 Images acquisition

X-ray microtomography images were acquired on the ID19 beamline at ESRF (European Synchrotron Radiation Facility), Grenoble (France). The acquisition was done in white beam configuration, using a ROI of 2048×1690 pixels. The sample was placed at 1.7 m and different filters were used in this configuration (2.8 mm of Al and 0.35 mm of W) to achieve an energy of 71.1 keV with a gap of 57. The voxel size was $7.42\,\mu\mathrm{m}^3$. We acquired 4998 radiographies in 360°, 41 references and 20 dark images to reduce the noise during the 3-D reconstruction. The acquisition time for each radiography was 0.25 s which induces a total acquisition time for the entire sample (two scan steps) of about 1 h (taking the motor movements into account). Two 3-D images were acquired: one for the sample before percolation experiment and one after, respectively named $\mathrm{Bvl_{be}}$ and $\mathrm{Bvl_{af}}$.

2.2.2 Image processing and parameter extraction

Analysis of the XMT images allows us to quantify the volume and morphology of the pore structure identified during the segmentation process. Using the 3-D pore representation, one can estimate its total and connected porosity and geometrical properties, such as its surface area and pore-size distribution. The processed images and results were mostly computed with Voxaya's software. The same methodological framework was applied to both images.

Filtering and region of interest extraction

The very first step in the image processing workflow consists in isolating the region of interest: a cylindrical mask is applied on the image in order to extract its relevant part. A median filter is then used to remove noise while preserving edges of the structures.

Segmentation and porosity calculation

Segmentation is one of the most important step in image analysis. It consists in gathering voxels that belongs to a same object and assigning them a single common value (see Fig. 1 which illustrates the segmentation step). Voxels identified to the matrix constitute the solid phase which have the highest intensity and appear in the brightest grey levels. Pores measured to be larger than the voxel size (here 7.42 µm) are entirely captured by the camera and appear in darkest grey levels in the image, forming a phase referred to as void phase or resolved porous phase. We name sub-resolved porous space the area appearing in intermediate grey levels and formed by matrix (calcite in the present case) and pores measured to be smaller than the voxel size. Note that this phase is sometimes denoted by the ambiguous term "microporous phase" whereas resolved porous phase is often called "macroporous phase". Presence of pores smaller that the voxel size can be confirmed for example by microscopic observations on thin sections or a priori knowledge of the rock.

In terms of numerical core analysis, computing porosity requires to determine the relative fraction of the void phase volume and to estimate the pore volume in the sub-resolved porous space. A first segmentation algorithm based on a region growing method was used to isolate the void phase. An additional image segmentation was then conducted to isolate the sub-resolved porous space and compute its volume fraction in the sample voxel. We can define the sample sub-resolved porosity Φ_S as follows:

$$\Phi_S = \xi_x \ \Phi_x, \tag{7}$$

where ξ_x and Φ_x respectively denote the volume fraction and the porosity of the sub-resolved porous space. The total porosity is then given by the following:

$$\Phi_T = \Phi_R + \Phi_S, \tag{8}$$

where Φ_R is the sample resolved porosity (that is, the volume fraction of the void phase). Assuming that the sample is chemically homogeneous, it is possible to estimate Φ_x. We first compute the mean greyscale values corresponding to solid and void phases, respectively denoted by G_m and G_v. Following (Mangane et al., 2013) and (Luquot et al., 2014a), the grey level value G_x of a voxel belonging to the sub-resolved porous phase is linearly related to Φ_x as follows:

$$\Phi_x = (G_m - G_x)/(G_m - G_v). \tag{9}$$

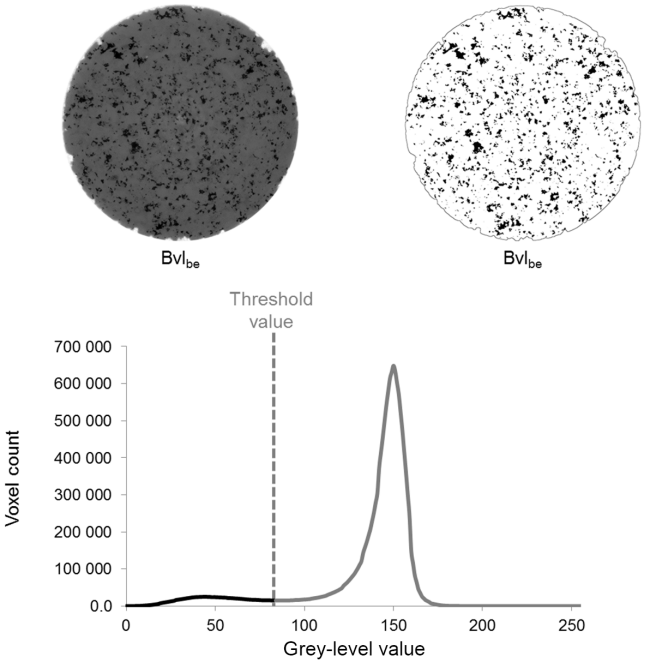

Figure 1. Histogram of grey scale values of Bvl sample images before the dissolution experiment. The threshold value n is indicated in the graph. On the top, a 2-D slice of Bvl before the dissolution experiment illustrates the pore initial pore structure on the left and the binary image next to the threshold step on the right.

Evaluating errors in porosity calculation

Estimating the uncertainty occurring in the porosity calculation can be achieved from an XMT image by performing, for example, several image segmentation with different, but close, input parameters and then calculating the associated porosities. For instance, if an image is segmented using a basic thresholding technique, then one can perform extra segmentations by varying threshold values by one or two units and computing the associated porosities. This enables to assess the robustness of the segmentation parameters determined by the user.

Connected components of the pore space

A clustering algorithm derived from (Hoshen and Kopelman, 1976) enables to assess the connectivity of the pore space by identifying neighbouring voxels that are connected to one another and assigning a distinct label to each connected component. In this study, the largest connected components of the pore space were extracted for both resolved and sub-resolved porosity.

Geometric parameters

Many geometric parameters can be computed from the segmented image of the pore space, namely the interface sur-

face area, its global curvature, and the Euler characteristics (Mecke, 2000; Vogel et al., 2010). Here, we focused on the pore-size distribution and the surface-to-volume ratio sometimes referred as "specific surface".

The imaged pore space is used to quantify pore network characteristics such as pore size. The pore-size distribution is evaluated from XMT images using a Voxaya module. According to Coker and Torquato (1995), the pore-size distribution function gives the probability that a random point in the pore phase lies at a distance x and $x + \mathrm{d}x$ from the nearest point on the pore–solid interface. This is achieved by computing the Euclidean distance from each voxel of the pore space to the interface, using a distance transform algorithm based on Meijster et al. (2002). Equivalently, one can consider this distance to be the radius of the largest sphere centred at this voxel and inscribed in the pore space. Yet, each sphere that is fully included in a larger one have no significant contribution to the pore space geometry and can thus be removed. In other words, this method returns the count of inscribed spheres that are maximal in the sense of inclusion.

Statistical measurements such as chord-length distribution functions (Torquato, 2002; Luquot et al., 2014a) were also calculated. The chord-length distribution function is linked to a probability density of random chords corresponding to a virtual mean pore diameter depending on each x, y, and z direction. It thus provides information on the sample anisotropy.

Diffusion coefficient

Diffusion experiments can be simulated on the void space image following the methodology described in Sen (2004). Consider a large number N of (virtual) diffusing particles, initially uniformly distributed in the void phase, and randomly moving following a Brownian motion, the diffusion coefficient $D(t)$ characterizes their ability to disperse in the void phase, probing its structure. We denote by $x_i(t)$ the position of the ith particle at time t and $\sigma(t)^2$ their mean square displacement, that is:

$$\sigma(t) = \frac{1}{N}\sum_{i=1}^{N}(x_i(t) - x_i(0))^2, \quad (10)$$

Then according to Einstein (1956):

$$\sigma(t)^2 = 6D(t)t. \quad (11)$$

If d_0 denotes the diffusion coefficient in an unbounded domain and τ the tortuosity, then when $t \to \infty$, $D(t)$ tends to an asymptotic value $D \approx d_0/\tau$.

Skeleton and properties

The skeleton of a three-dimensional object is a one-dimensional reduction, centred inside this object, preserving its geometrical and topological features. It provides a simplified representation of a shape: the skeleton of a cylinder, for instance, consists of its axis of rotational symmetry. Formal definitions can be found in Siddiqi and Pizer (2008).

The skeleton is particularly known to be a tool of great interest to investigate large objects with complex geometry, such as large microtomography images of porous media. An implementation of the classical thinning algorithm described in Lee et al. (1994) was used for this work.

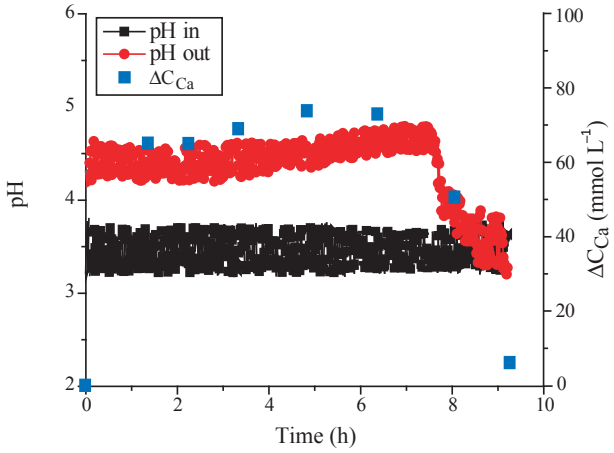

Figure 2. Inlet (black) and outlet (red) pH variation during the percolation experiment as well as variation in calcium concentration(blue).

3 Results

The temporal evolution of the increase in calcium concentration, ΔC_{Ca}, during the percolation experiment as well as the inlet and outlet fluid pH are presented in Fig. 2. Dissolution reaction occurred during the percolation experiment. Indeed, the ΔC_{Ca} is always positive ($\Delta C_{Ca} > 0$) indicating Ca release in the outlet fluid. Moreover, the outlet pH (Fig. 2) is higher than the inlet one which corroborates proton consumption and thus calcite dissolution (Reaction R1). Dissolution reaction may induce porosity increase and other geometrical, structural and hydrodynamical parameter changes. Evaluating and characterizing these changes are essential for developing predictive models of reactive-transport processes such as those occurring during CO_2 geological storage, fracking processes, oil and gas exploitation, acid mine drainage, or seawater intrusion among others.

3.1 Laboratory petrophysical parameters

3.1.1 Porosity evolution

Initial porosity measurements on sample Bvl_{be} were performed by the triple weighing method (TW) and give us an initial porosity $\phi_{i(TW)}$ of 16.06 ± 0.44 % (4 measurements), which is slightly higher than the one provided by the quarries miner companies. This porosity is the connected porosity which only takes into account the open pores connected to one of the sample surface. After the dissolution experiment, the same methodology was applied four times and we measured a final porosity $\phi_{f(TW)} = 20.26 \pm 0.73$ %.

Mass balance calculation from the dissolution experiments were performed using Eqs. (5) and (6) and the final porosity was evaluated using the initial porosity $\phi_{f(chem)}$ using the initial porosity $\phi_{i(TW)}$ and the ΔC_{Ca} presented in Fig. 2. We obtained a final porosity $\phi_{f(chem)} = 19.37 \pm 0.56$ % (propagating the error of the TW method on the initial porosity value and the one from the chemical analysis). The slightly higher increase in porosity, measured by the TW method, can be explained by the connection of initially non- connected pores to the new connected porosity resulting from the dissolution process whereas the porosity calculated by the mass balance is affected by the dissolution only. The different porosity measurements and calculations are summarized in Table 2.

3.1.2 Pore-size distribution

We obtained the pore-size distribution for sample Bvl before and after the dissolution experiment from the retention curve (RET) as explained in Sect. 2.1.2. We measured the retention curve by draining the sample both in the flow and counter-flow direction in order to evaluate the pore-size anisotropy. If the pore-size distribution was heterogeneous, then we should get different retention curves due to the gradient of capillary pressure inside the sample. Specifically, large pores at the inlet (but not at the outlet) will desaturate at small suctions applied to the inlet (i.e., for small rpm when the inlet is placed outside in the centrifuge). Reversely, if the sample is rotated, those pores will only desaturate when suction is large enough to drain any of the outlet pores. The net result is that the measured curve will exhibit directional dependence as previously observed by Luquot et al. (2014b).

Initially, the pore-size distribution is homogeneous; the initial retention curves are similar in both sample orientations (Fig. 3). After the dissolution experiment, due to calcite dissolution and porosity increase, the retention curves vary from the initial one. Moreover, we can observe in Fig. 3, that after the dissolution experiment, some heterogeneity appeared along the sample inducing different shapes for the retention curves acquired in both directions. The corresponding pore-size distributions are presented in Fig. 4.

The results show that after dissolution, the amount of pores of radii larger than 102.27 µm increases drastically.

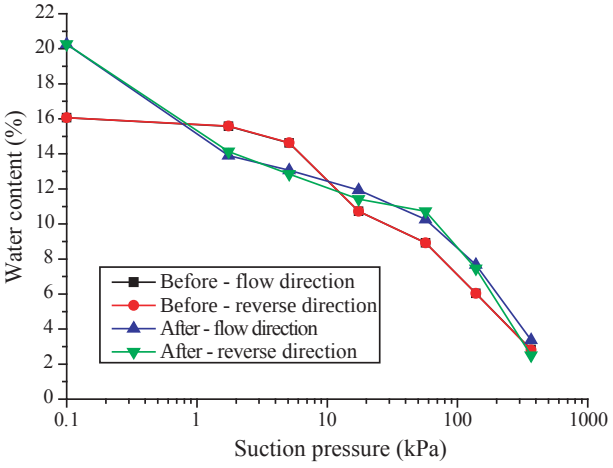

Figure 3. Retention curves before and after the dissolution experiment for sample Bvl.

The increase in largest pore size is similar whatever the sample direction indicating that these pores are well connected together and broke through the sample. We can also observe (Fig. 3) that the second major difference between the retention curves before and after dissolution appears for pore radii $10.23 < r_p < 34.99$ µm (suction between 5.11 and 17.47 kPa). After the dissolution experiment, fewer pores of such radii are present through the sample, indicating that most of the dissolution occurred in these pores.

The results also display some differences in the pore-size distribution after the dissolution experiment depending on the sample orientation. These differences highlight some heterogeneous dissolution inducing different pore diameter changes along the sample. They are however minor when compared with other experiments with strong dissolution localization (Luquot et al., 2014a). Most discrepancy is visible for intermediate and smallest pores ($0.48 < r_p < 10.23$ µm). Moderately large pores (radius around 10 µm, suction at 17.47 kPa) are better connected to the inlet than to the outlet (that is, they drain better when the sample is placed opposite to the flow direction, i.e., dragging toward the inlet, than otherwise). The proportion of the smallest pores is consistently lower when the sample is placed opposite to the flow direction, implying that dissolution also occurred in these pores at the inlet. However, the water contents obtained with the sample placed in the flow direction for high suctions (small pore sizes) were higher than before the experiments, implying a small decrease in pore size at the outlet.

3.1.3 Diffusion coefficient

Figure 5 displays the results of the two iodide diffusion experiments performed before and after the dissolution experiment on sample Bvl. The curves show the time evolution of iodide at the sink reservoir, which is proportional to the cumulative mass of iodide that has diffused through the sam-

Table 2. Determined porosities [%] (final one by mass balance calculation (chem), before and after by triple weighing technique (TW), and before and after as well as total (tot.), effective (open), resolved (res.) and sub-resolved (subres.) by XMT images (XMT)), effective diffusion coefficients D_{eff} [$m^2 s^{-1}$] (from through laboratory experiment (I^-) and XMT images (XMT)), permeability k [m^2] and total fluid–rock interface (from BET measurement and XMT images (Minko)) for samples Bvl_{be} and Bvl_{af}.

	$\phi_{(TW)}$ %	$\phi_{(XMT)}$ %				$\phi_{(chem)}$ %	$D_{eff(I^-)}$ $m^2 s^{-1}$	$D_{eff(XMT)}$ $m^2 s^{-1}$	k m^2	$S_{(BET)}$ $m^2 g^{-1}$	$S_{(Minko)}$ $m^2 g^{-1}$
		res.	subres.	tot.	open						
Bvl_{be}	16.06	10.42	6.71	17.13	15.94	–	1.43×10^{-12}	3.75×10^{-12}	4.01×10^{-14}	0.3489	0.0018
Bvl_{af}	20.26	15.62	7.17	22.80	21.75	19.37	2.96×10^{-11}	2.26×10^{-11}	1.16×10^{-12}	–	0.0021

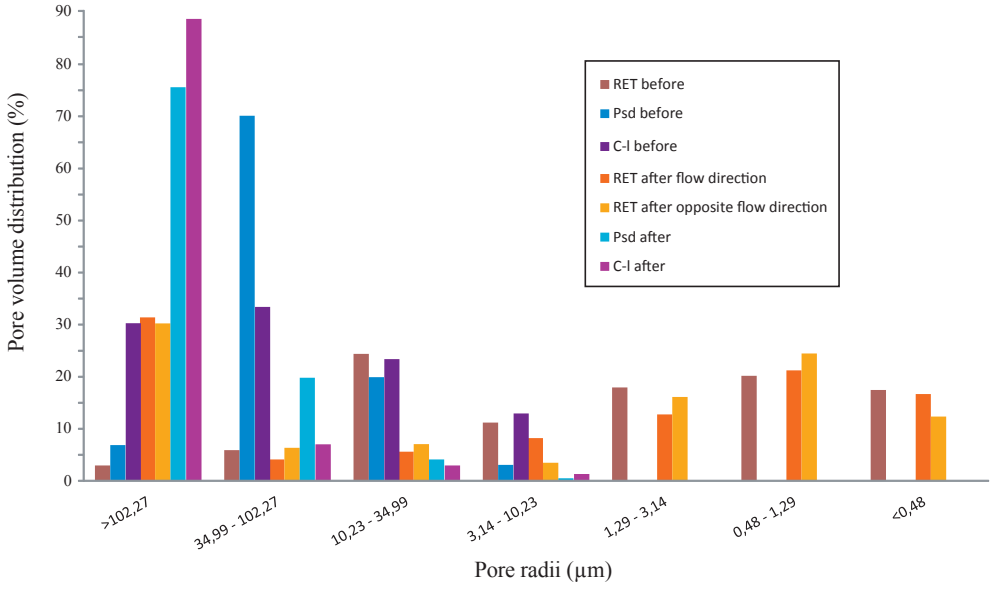

Figure 4. Pore volume content for different pore-size diameters before and after the dissolution experiment. The data have been extracted from the Psd and C-l numerical measurements and RET laboratory acquisition. For the latter, the distributions after dissolution were obtained both by draining in the flow direction and in the opposite direction.

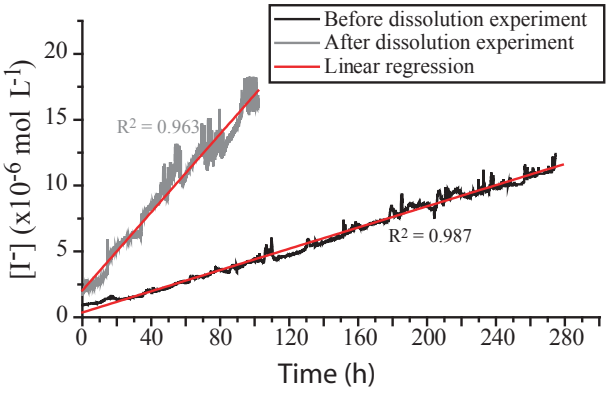

Figure 5. Iodine concentration measured in the sink cell during diffusion experiment through sample Bvl before and after the dissolution experiment.

ple Bvl until time t. Only the steady-state phase is reported here, when the iodide concentration in the sink cell increases linearly with time. Linear regression of the steady-state portion yields the effective diffusion coefficient (Eq. 2). Experimental results are summarized in Table 2. After the dissolution experiment, the diffusion coefficient is increased by 1 order of magnitude, as suggested by the noticeable increase in the slope of iodide increment after dissolution. This increase is linked to a decrease of the tortuosity coefficient τ from 14.43 (highly tortuous pore skeleton, see Fig. 6) to 3.57. These values of effective diffusion coefficients and tortuosity, as well as their evolution with dissolution, are coherent with other previous laboratory measurement done on limestone samples (Boving and Grathwohl, 2001; Gouze and Luquot, 2011; Casteleyn et al., 2011; Peng et al., 2012; Luquot et al., 2014b).

3.1.4 Permeability change

The changes in the sample permeability with time $k(t)$ induced by the dissolution experiment is reported in Fig. 7. Unsurprisingly, permeability increases due to calcite dissolution, as previously mentioned by other authors (Fredd and Fogler, 1998; Luquot and Gouze, 2009; Noiriel et al., 2009; Elkhoury et al., 2013; Carroll et al., 2013). The permeability increase rate ($\mathrm{d}k/\mathrm{d}t$) changes drastically at $t \approx 8$ h, which is surely associated with the breakthrough of the main dissolution path (wormhole).

3.2 XMT analysis

3.2.1 Porosity evolution

The total porosity calculated from the XMT images, on sample $\mathrm{Bvl_{be}}$ (before dissolution) and $\mathrm{Bvl_{af}}$ (after dissolution) is 17.13 and 22.80 %, respectively. As explained in the methodology section, several steps have been performed with similar parameters in order to estimate the possible error of assessment on this crucial step. We used five different segmentation results to calculate the resolved porosity before and after the dissolution experiment. The results are presented in Table 3. We can observe that decreasing the thresholding value for the sample $\mathrm{Bvl_{be}}$ induces a resolved phase underestimation up to 13 % whereas increasing the threshold value only causes an overestimation less than 0.5 %. These calculations indicate that the smallest threshold values were used to estimate the resolved phase volume avoiding huge underestimations. After the dissolution experiment, an error (± 1 and 2) on the thresholding n value carries out fewer changes on the resolved phase estimation. Increasing and decreasing by 1 the threshold n value after the dissolution experiment has no effect on the resolved phase estimation (error always lower than 0.26 %). Consequently, all the calculations done on the XMT images were performed using the segmented images obtained by setting the threshold value to n.

Initially, the total porosity calculated on sample $\mathrm{Bvl_{be}}$ is characterized by 60.82 % of large pores (resolved porosity) and 39.18 % of small pores, lower than the voxel size (sub-resolved porosity). After the dissolution experiment, the total porosity is mainly characterized by a high amount of large pores (resolved porosity) which represents 68.51 % of the total porosity (see Table 3). The total porosity increase is thus mainly controlled by the increase of the resolved porosity. Figure 8 shows the resolved and sub-resolved porosities for samples $\mathrm{Bv_{lbe}}$ and $\mathrm{Bv_{laf}}$ along the sample length (which corresponds to the flow direction during the dissolution experiment). We can observe that both resolved and sub-resolved porosity increase along the sample length. These porosity increases are homogeneous along the sample except for the first millimetres of the sample where the resolved porosity increase faster than in the remaining part of the sample. The same phenomenon is observed for the sub-resolved porosity,

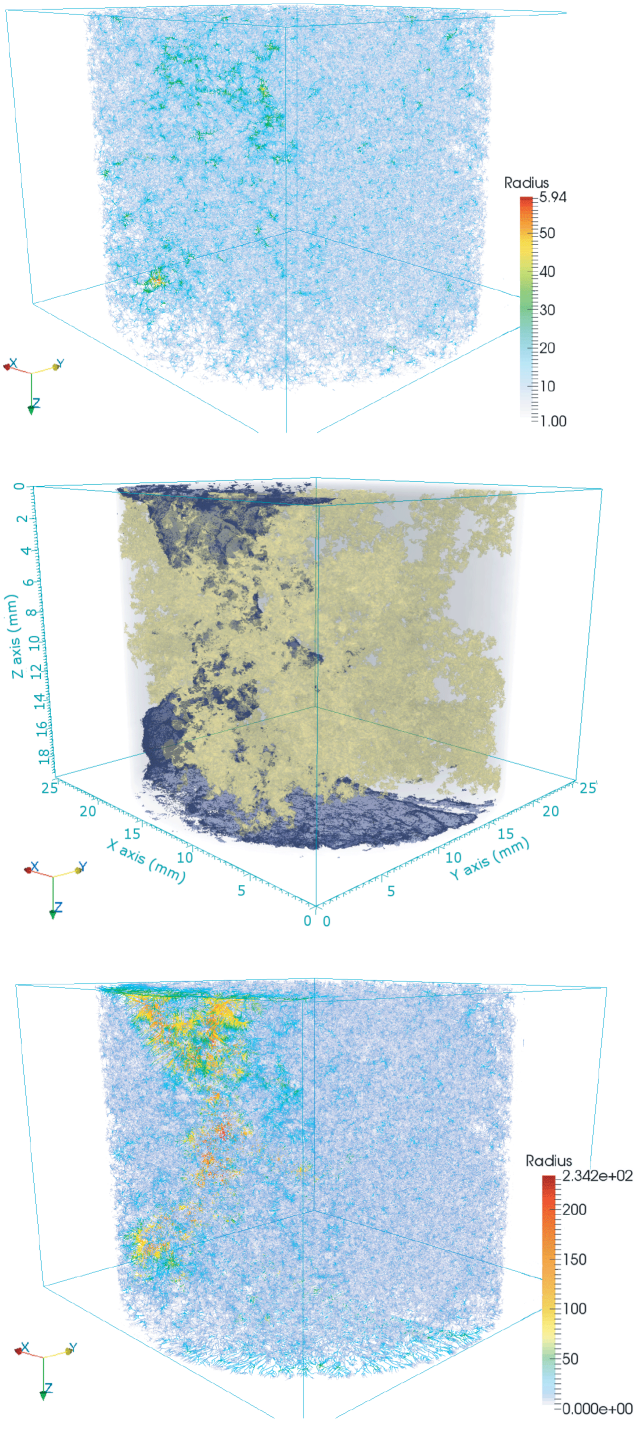

Figure 6. From top to bottom: extracted skeleton on sample $\mathrm{Bvl_{be}}$, the formed wormholed in sample $\mathrm{Bvl_{af}}$ (blue) replaced in sample $\mathrm{Bvl_{be}}$ where the resolved connected porosity appears in yellow, extracted skeleton on sample $\mathrm{Bvl_{af}}$. For the extracted skeleton images, the blue to red scale colours corresponds to pore-size increase indicated in pixels (up to 60 pxls for sample $\mathrm{Bvl_{be}}$ and 234 pxls for sample $\mathrm{Bvl_{af}}$).

Table 3. Sensitivity analysis of the threshold value n value on the relative fraction of the resolved phase volume (RPV [%]) for samples Bvl_{be} and Bvl_{af} with the relative error ζ [%].

	n	$n-2$		$n-1$		$n+1$		$n+2$	
	RPV (%)	RPV (%)	ζ (%)	RPV (%)	ζ (%)	RPV (%)	ζ (%)	RPV (%)	ζ (%)
Bvl_{be}	10.42	9.06	−13.05	9.39	−9.82	10.42	0.00017	10.46	0.44
Bvl_{af}	15.62	15.17	−2.90	15.61	−0.06	15.66	0.26	16.84	7.81

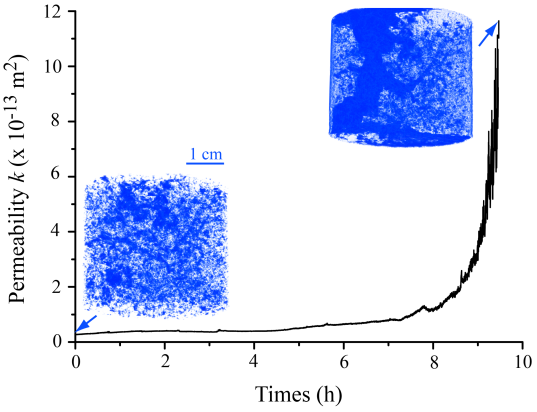

Figure 7. Time evolution of permeability k during dissolution experiment of sample Bvl. The corresponding 3-D images of the resolved porosity for sample Bvl_{be} and Bvl_{af} are reported for the initial and final percolation times.

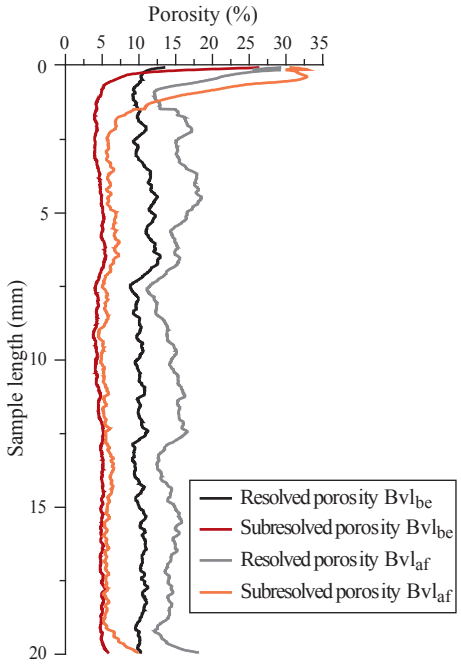

Figure 8. Porosity changes along samples Bvl_{be} and Bvl_{af}. Both resolved and sub-resolved porosities are plotted.

where its increase is higher for the first 2 mm of the sample. Similar trends of porosity increase due to carbonate dissolution have been monitored by previous authors. Nevertheless, no conclusion on the dissolution patterns can be proposed as Luquot and Gouze (2009) and Menke et al. (2015) linked the homogeneous porosity increase profile to homogeneous dissolution whereas Smith et al. (2013) and Luquot et al. (2014a) observed wormhole formation. These versatile conclusions are due to the complex structure and pore geometry of the different limestone samples used. Visualising 3-D XMT images, we can conclude that during the Bvl dissolution experiment a wormhole was formed, which promoted a homogeneous porosity increase along the sample.

One of the advantages of using 3-D XMT images is the ability to distinguish the total porosity from the effective one, or in other words from the connected porosity. Performing a connectivity computation, we can evaluate which part of the total porosity is actually contributing to the fluid flow. Table 4 indicates the volumes of the resolved and sub-resolved phases are indicated as well as the volume of the connected resolved and sub-resolved phases with the corresponding fraction of the connected part. We can observe that initially, the sample is mainly connected through the sub-resolved phase, but after the dissolution experiment the resolved porous phase becomes more connected and mostly contribute to the fluid pathway. This increase in connectivity through the resolved porous phase can be linked to the wormhole formation which represents 71.47 % of the connected resolved porous phase. Various other small clusters compose the percolating resolved phase but none of them is larger than 2 % of the total porous volume. The main connected path after the dissolution experiment is imaged in Fig. 6.

3.2.2 Pore-size distribution

The pore-size distribution of the resolved porous phase was calculated for sample Bvl_{be} and Bvl_{af} using two different methodologies. We calculated the pore-size distribution (Psd) as explained in Sect. 2.2.2, computing the radius of the largest inscribed sphere centred at every point of the pore space, provided it is maximal for inclusion. We also estimated an equivalent pore-size distribution by performing statistical measurement and calculating the chord-length distribution functions (C-l). The chord-length distribution func-

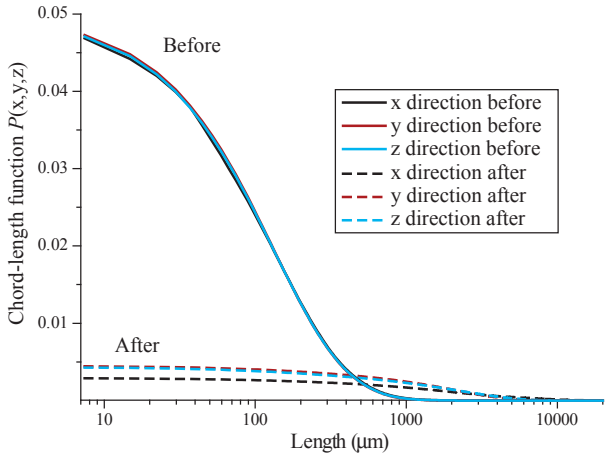

Figure 9. Chord-length function along x, y and z ($P(x, y, z)$) for sample Bvl before and after the dissolution experiment.

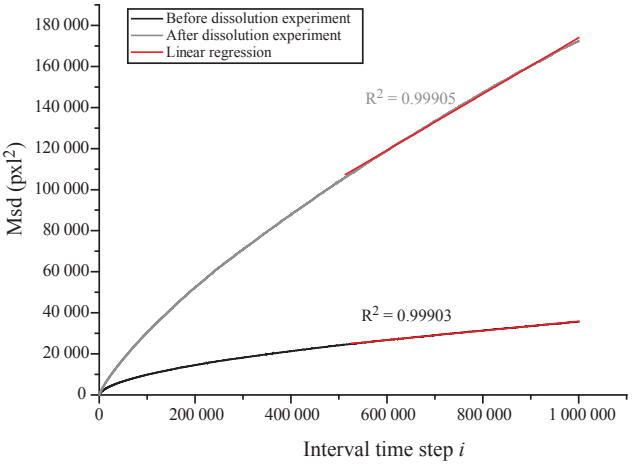

Figure 10. Porosity change along samples Bvl_{be} and Bvl_{af}. Both resolved and sub-resolved porosities are plotted.

tions for sample Bvl_{be} and Bvl_{af} are plotted in Fig. 9 for the 3 directions (x, y, z). Results from both methodology (Psd and C-l) are summarized in Fig. 4 where the pore volume distribution is scaled according to the experimental RET thresholds.

Figures 4 and 9 show that initially, the sample is mainly composed of pores having small and intermediate diameters. Most of the pores are smaller than 204.5 µm (69.73 %) in diameter and no anisotropy is observed. After the dissolution experiment, the chord-length distribution evolved and a certain anisotropy appears. In sample Bvl_{af}, the amount of small to intermediate pore diameter decreased significantly to 11.27 % of pores smaller than 204.5 µm in diameter. Larger pores were formed due to the dissolution process. A significant amount of pores presenting diameters comprised between 1 and 3 mm are measured and pores having a diameter up to 20 mm in the x direction can be found. It corresponds to the local face dissolution at the sample inlet inducing large porosity increase (Figs. 8 and 6).

The pore-size distribution (Psd) presents similar results than those obtained by the chord-length function. Some discrepancies are observed for sample Bvl_{be} for the largest pore diameter. With the Psd analysis, the highest pores have a diameter comprised between 70 and 204.5 µm, whereas with the chord-length function, we calculated initially lower proportion of these pores and a higher one for the largest pores (diameter higher than 204.5 µm).

3.2.3 Diffusion coefficient

The effective diffusion coefficient $D_{eff(XMT)}$ before and after dissolution is obtained by computing randomly distributed particles in the rock pores following the method describe in Sect. 2.2.2. Figure 10 displays the results of the two computations performed on Bvl_{be} and Bvl_{af}. The curves show the mean squared displacement (Msd) for an interval time step i. For large time steps, the Msd is linearly dependent to the effective diffusion coefficient (Einstein, 1956). Linear regression of the steady-state portion yields the effective diffusion coefficient. The obtained effective diffusion coefficient for Bvl_{be} and Bvl_{af} are summarized in Table 2. As expected and previously reported in the literature (Gouze and Luquot, 2011; Luquot et al., 2014b), the effective diffusion coefficient increases after limestone dissolution experiments.

4 Comparison and discussion

This section compares the different parameters characterized using, on the one hand, classical laboratory measurements and on the other hand, XMT images. We first compared laboratory measurements and computational analysis duration for each parameter, in order to evaluate which approach is the most time consuming. The complete image processing described in Sect. 2.2.2 was performed on a workstation equipped with two quad-core Intel Xeon CPU X5560 @2.80 GHz and 192 GB DDR3 RAM. We can observe in Fig. 11 that globally, even if the computer used here is not a high end build, the total analysis time for Bvl_{be} and Bvl_{af} is much shorter using image processing than the time analysis for performing laboratory measurements. The total time needed to extract the different parameters discussed in this article from the XMT images is 23 days, whereas the time required to determine the same parameters using laboratory measurements is 60 days. Moreover, some specific processing (namely skeletonization) were performed using basic, non-optimized implementations of classical algorithms that can be found in open source software packages such as ImageJ. Besides, in most cases, data extracted from XMT images provided more information than the desired parameters studied in this article. Considering porosity, only effective porosity can be determinated by the experimental triple

Table 4. Resolved (RPV) and total (TPV) phase volume [mm^3] and connected resolved (connected-RPV) and total (connected-TPV) phase volume [mm^3] with the respective connected resolved (connected-RF) and total (connected-TF) fraction [%].

	RPV (mm^3)	connected-RPV (mm^3)	connected-RF (%)	TPV (mm^3)	connected-TPV (mm^3)	connected-TF (%)
Bvl_{be}	1007.76	380.90	37.80	1856.53	1727.78	93.07
Bvl_{af}	1511.34	1080.18	71.47	2432.96	2321.12	95.40

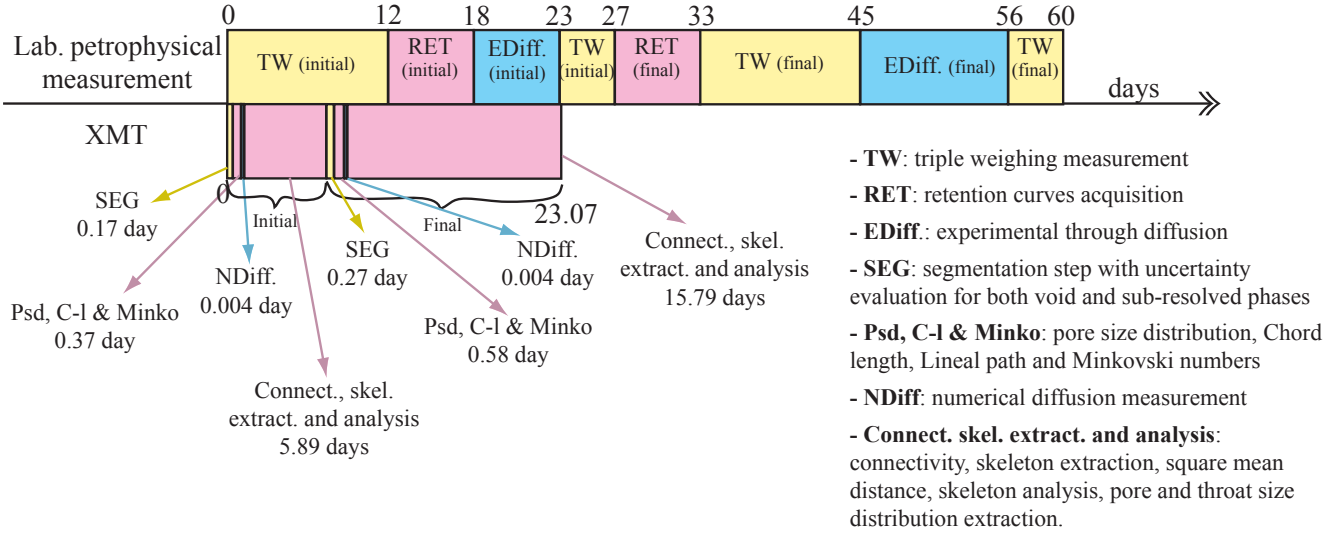

Figure 11. Time scale of the different methods used in this study for both laboratory and XMT images approaches.

weighing method, whereas both effective and total porosities can easily be calculated from the XMT images. Total porosity can be a key parameter when chemical processes such as dissolution occurred. The final porosity closely depends on the initial effective porosity, the porosity created by dissolution and part of the initially closed porosity that the dissolution process made accessible. Porosity determination with helium pycnometry is a fast and non-destructive alternative not used in this study.

However, the main drawback of the XMT image analysis is the high dependence of all parameters on the voxel size. When using different laboratory techniques to measure the desired parameters, various resolution scales can be achieved. For example, the total fluid–rock interface determined by BET measurement has higher resolution than the one determined by XMT images. Specifically, the grain roughness as well as grains smaller than the XMT resolution (7.42 µm) cannot be measured and the water–rock interface area is underestimated a priori.

Nevertheless, for most of the determined parameters, good agreement is observed between the data computed from XMT images and the data measured experimentally. As observed in Table 2, the initial porosity determined by the triple weighing method is only different from the effective porosity extracted from XMT images by 0.74 %. After the dissolution experiment, the estimated porosity is quite similar even if the difference is more important. The final porosity determined by the mass balance calculation is the lowest one ($\phi_{f(chem)} = 19.37 \pm 0.56$ %). As explained before, the slight difference between the porosity obtained by triple weighing and mass balance calculation can be explained by the connection of initially non-connected pores to the new connected porosity by the dissolution process. Actually, the porosity calculated by the mass balance is only affected by dissolution. In this case, if only initial effective porosity and mass balance are used, the final porosity can be underestimated. Indeed, as observed in Fig. 12 a volume of 32 mm^3 of non-connected pores is initially present in the final wormhole feature. The porosity measured by the triple weighing method is smaller than the one estimated from the XMT images. This difference can be due to the formation of highly connected pathways (wormholes) percolating the entire core. This very permeable fluid pathway in the sample after the dissolution experiment represents an important water leak pathway where some water can flow out of the sample, leading to an underestimation of the saturated sample weighing. Regarding porosity measurement and analysis, we can conclude that porosity calculated from the XMT images is the most reasonable, as we can distinguish the effective one from the total one. Moreover the time required to calculate the XMT

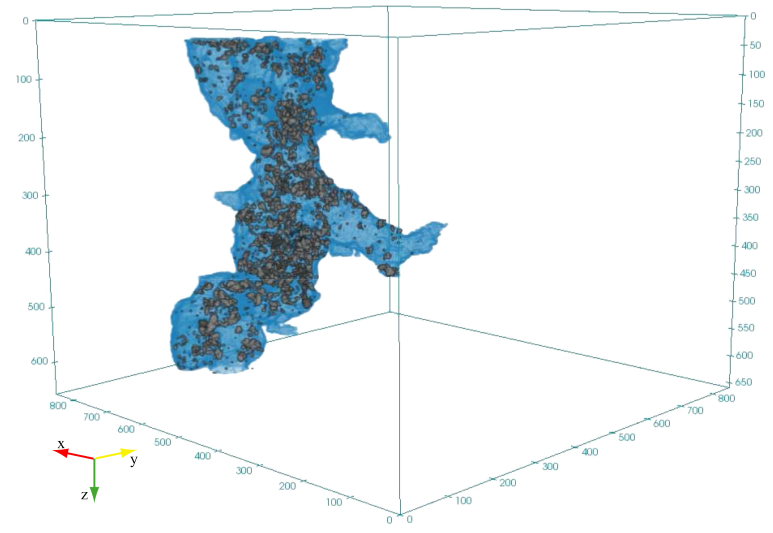

Figure 12. 3-D image of the formed wormhole (blue) and initial non-connected porosity presented in the final wormhole feature (grey).

porosities is much shorter than the one needed by the triple weighing method.

The same conclusion cannot be drawn for the pore-size diameter distribution. For this parameter, the retention curves acquisition allows to classify pores with diameters smaller than the XMT images voxel size (7.42 µm). Figure 4 displays the pore-size distributions before and after the dissolution experiment determined by three different methods: measuring the retention curves of the core sample via laboratory experiments (RET), calculating the larger sphere inscribed in the pore space (Psd) and measuring the chord-length distribution function (C-l) on the XMT images. As already mentioned, we can see that the pore-size distribution obtained by the retention curves analysis allows to determine the quantity of pore with radii down to 0.48 µm. Results from Psd and C-l are quite similar. In sample Bvl_{be}, the C-l methods determined a higher amount of very large pores, whereas the Psd methods estimated larger content of pores with radii comprised between 34.99 and 102.27 µm. After the dissolution experiment, for both techniques based on the XMT images the fraction of the largest pores increases significantly. This increase of the amount of large pore is in agreement with the dissolution process and the formation of a preferential flow path (wormhole). Comparing with the RET method, we observed that the RET pore-size distribution underestimates the largest pores and the smallest pores are certainly overestimated. This large difference can be attributed to the basic definition of a pore (Nimmo, 2004; Hinai et al., 2014). Indeed, during retention curves measurement, the volume of pore estimated for a given suction pressure correspond to the volume of extracted water through a corresponding throat. Consequently, this laboratory technique gives a mixed estimation between pore and throat distribution, underestimating the largest pores and overestimating the smallest ones. It might be interesting to simulate drainage and imbition experiments using the XMT images as previously done by Knackstedt et al. (2006) and Prodanovic et al. (2010) in order to compare the laboratory RET measurements in a further study. To summarize, one should note that the pore-size distribution obtained by the retention curves indicates the capillary pressure needed to extract a specific fluid volume, but without any information about the amount of pores containing this fluid volume and the respective pore diameters. The two other methods used here to extract the pore-size distribution using the XMT images allow us to determine the pore-size diameter at each voxel point with some anisotropy information (C-l technique). Nevertheless, with these two methods, we don't have any knowledge about the connectivity and the accessibility to these pores. Using the extracted skeleton, we can extract both pore and throat distributions and localize them in the 3-D sample. This fourth method gives the best pore and throat size distribution and their localization (Fig. 6).

The third main parameter measured experimentally and using XMT images is the effective diffusion coefficient. By the utilization of a laboratory through diffusion experiments, determination of the diffusion coefficient is time consuming (Fig. 11) and strongly depends on sample length as the diffusion time increases with the squared length. Using the XMT images, the calculation of the effective diffusion coefficient is very efficient and performed in less than 9 min. The results of both methods are presented in Table 2. The values obtained by laboratory measurements and statistical modelling are similar. With both techniques, the effective diffusion coefficient increased after the dissolution experiment by 1 order of magnitude. Consequently, the tortuosity coefficient decreased after the dissolution experiment and both values for Bvl_{be} and Bvl_{af} are similar for laboratory measurements and

image based computations. The statistical estimation using XMT images is a good option to determine the effective diffusion coefficient as the time needed is 1500 times faster than the utilization of a laboratory through diffusion experiments.

5 Conclusions

In this paper, we have shown that microtomographic imaging hardware and computational techniques have progressed to the point where properties such as effective diffusion coefficient, conductivity and pore-size distribution can be calculated on large three-dimensional digitized images of real core rock sample. We demonstrated that for most of the parameters studied here, the values obtained by computing XMT images are in agreement with the classical laboratory measurements. For some parameters, such as the porosity, the computational one is the more informative, as one can calculate both total and effective porosity. As discussed here, when dissolution process occurs, the knowledge of the total porosity can be necessary. As the definition of pore is highly discussed in the scientific community, we observed that the pore-size distributions obtained by XMT images and laboratory experiments are slightly different. We highlighted advantages and limitations of both approaches: the RET measurement allows to determine the accessible volume for a given capillary pressure, whereas Psd and C-l methods extract the maximum pore volume locally without information of its accessibility. Concerning the effective diffusion coefficient, we observed that both approaches are valuable and similar results are obtained. Nevertheless, the duration of a laboratory through-diffusion experiment is much longer than the time required by the computational option (about 1500 times longer).

As a conclusion, computing XMT images to determine transport, geometrical, and petrophysical parameters provide similar results than the one measured at the laboratory in only 23 days instead of 60 days for the laboratory option. Moreover, the studied sample presents both resolved and subresolved porosities, which would be the case for any other type of natural or synthetic porous material, whatever the acquisition technique. Thus, the framework developed in this work is relevant and can be easily applied in many contexts.

Furthermore, new developments are expected in a near future favouring microtomographic imaging at higher resolutions with faster acquisition times allowing dynamical effects to be imaged, (Bultreys et al., 2015; Douissard et al., 2012; Landry et al., 2014). Further developments using the extracted skeleton will also allow us to extract the accessible pore volume and the capillary pressure needed to ingress.

Acknowledgements. We would like to acknowledge Arnaud Chabanel from EURL Thomann Hanry (Carriéres de Vers Est) to provide us the rock sample and Paul Tafforeau from ESRF for the X-ray microtomography images acquisition. L. Luquot is funded by the Juan de la Cierva fellowship (MINECO, Spain).

Edited by: H. Steeb

References

Adamson, A. W. and Gast, A. P.: Physical Chemistry of Surfaces, Wiley, New York, 1997.

Alshibli, K. A. and Reed, A. H. (Eds.): Advances in Computed Tomography for Geomaterials: GeoX 2010, Wiley, New York, 2012.

Archie, G. E.: The electrical resisitivity log as an aid in determining some reservoir characteristics, Soc. Petrol. Eng., 146, 54–62, doi:10.2118/942054-G, 1942.

Arns, C., Knackstedt, F., M., and Pinczewski, W.: Accurate estimation of transport properties from microtomographic images, Geophys. Res. Lett., 28, 3361–3364, 2001.

Arns, C., Knackstedt, M., Pinczewski, W., and Garboczi, E.: Computation of linear elastic properties from microtomographic images: methodology and agreement between theory and experiment, Geophysics, 67, 1396–1405, 2002.

Arns, C., Bauget, F., Ghous, A., Sakellario, A., Senden, T., Sheppard, A., Sok, R., Pinczewski, W., Kelly, J., and Knackstedt, M.: Digital core laboratory: petrophysical analysis from 3D imaging of reservoir core fragments, Petrophysics, 46, 260–277, 2005a.

Arns, C., Bauget, F., Limaye, A., Sakellariou, A., Senden, T., Sheppard, A., Sok, R., Pinczewski, W., Bakke, S., Berge, L., Oren, R., and Knackstedt, M.: Pore-scale characterization of carbonates using X-ray microtomography, SPE J., 10, 475–484, 2005b.

Arns, C. H., Knackstedt, M. A., Pinczewski, W. V., and Martys, N. S.: Virtual permeametry on microtomographic images, J. Petrol. Sci. Geol., 45, 41–46, 2004.

Baker, S. and Friedman, G. M.: A non-destructive core analysis technique using X-rays, J. Sediment. Petrol., 39, 1371–1383, 1969.

Barrante, J. (Ed.): Applied Mathematics for Physical Chemistry, Prentice-Hall, Englewood Cliffs, New Jersey, 1974.

Becker, M. and Shapiro, A.: Interpreting tracer breakthrough tailing from different forced-gradient tracer experiment configurations in fractured bedrock, Water Resour. Res., 39, 1024, doi:10.1029/2001WR001190, 2003.

Bjerreskov, M.: Discoveries on graptolites by X-ray studies, Acta Palaeontol. Pol., 21, 463–471, 1978.

Boving, T. B. and Grathwohl, P.: Tracer diffusion coefficients in sedimentary rocks: correlation to porosity and hydraulic conductivity, J. Contam. Hydrol., 53, 85–100, doi:10.1016/S0169-7722(01)00138-3, 2001.

Bultreys, T., Boone, M., Boone, M., De Schryver, T., Masschaele, B., Van Hoorebeke, L., and Cnudde, V.: Fast laboratory-based micro-computed tomography for pore-scale research: illustrative experiments and perspectives on the future, Adv. Water Resour., 1–11, doi:10.1016/j.advwatres.2015.05.012, 2015.

Calvert, S. E. and Veevers, J. J.: Minor structures of unconsolidated marine sediments revealed by X-radiography, Sedimentology, 1, 287–295, doi:10.1111/j.1365-3091.1962.tb01151.x, 1962.

Carroll, S., Hao, Y., Smith, M., and Sholokhova, Y.: Development of scaling parameters to describe CO_2–rock interactions within Weyburn-Midale carbonate flow units, Int. J. Greenh. Gas Con., 16, S185–S193, doi:10.1016/j.ijggc.2012.12.026, 2013.

Casteleyn, L., Robion, P., David, C., Collin, P.-Y., Menendez, B., Fernandes, N., Desaubliaux, G., and Rigollet, C.: An integrated study of the petrophysical properties of carbonate rocks from the "Oolithe Blanche" formation in the Paris Basin, Tectonophysics, 503, 18–33, doi:10.1016/j.tecto.2010.09.031, 2011.

Cnudde, V. and Boone, M.: High-resolution X-ray computed tomography in geosciences: a review of the current technology and applications, Earth-Sci. Rev., 123, 1–17, doi:10.1016/j.earscirev.2013.04.003, 2013.

Coker, D. A. and Torquato, S.: Simulation of diffusion and trapping in digitized heterogeneous media, J. Appl. Phys., 77, 955–964, doi:10.1063/1.358940, 1995.

Crank, J.: The Mathematics of Diffusion, Oxford University Press, Ely House, London, 1975.

Cui, X., Bustin, R., and Dipple, G.: Selective transport of CO_2, CH_4, and N_2 in coals: insights from modeling of experimental gas adsorption data, Fuel, 83, 293–303, doi:10.1016/j.fuel.2003.09.001, 2004.

Cui, X., Bustin, A. M. M., and Bustin, R. M.: Measurements of gas permeability and diffusivity of tight reservoir rocks: different approaches and their applications, Geofluids, 9, 208–223, doi:10.1111/j.1468-8123.2009.00244.x, 2009.

Douissard, P.-A., Cecilia, A., Rochet, X., Chapel, X., Martin, T., Van De Kamp, T., Helfen, L., Baumbach, T., Luquot, L., Xiao, X., Meinhardt, J., and Rack, A.: A versatile indirect detector design for hard X-ray microimaging, J. Instrum., 7, P09016, doi:10.1088/1748-0221/7/09/P09016, 2012.

Dunsmuir, J., Ferguson, S., D'Amico, K., and Stokes, J. P.: X-ray micro tomography. A new tool for the characterization of porous media, SPE J., 22860, doi:10.2118/22860-MS, 1991.

Einstein, A.: Investigations on the Theory of the Brownian Movement, edited by: Furth, R., translated by: Cowper, A. D., Dover Publications, New York, 1956.

Elkhoury, J. E., Ameli, P., and Detwiler, R. L.: Dissolution and deformation in fractured carbonates caused by flow of CO_2-rich brine under reservoir conditions, Int. J. Greenh. Gas Con., 16S, S203–S215, doi:10.1016/j.ijggc.2013.02.023, 2013.

Espinoza, D. N. and Santamarina, J. C.: Water CO_2 mineral systems: interfacial tension, contact angle, and diffusion implication to CO_2 geological storage, Water Resour. Res., 46, W07537, doi:10.1029/2009WR008634, 2010.

Fick, A.: Ueber diffusion, Ann. Phys., 170, 59–89, 1855.

Fredd, C. N. and Fogler, H. S.: Influence of transport and reaction on wormhole formation in porous media, AIChE J., 44, 1933–1949, 1998.

Garing, C., Luquot, L., Pezard, P., and Gouze, P.: Electrical and flow properties of highly heterogeneous carbonate rocks, AAPG Bull., 98, 49–66, doi:10.1306/05221312134, 2014.

Gillham, R. W., Sudicky, E. A., Cherry, J. A., and Frind, E. O.: An advection–diffusion concept for solute transport in heterogeneous unconsolidated geological deposits, Water Resour. Res., 20, 369–378, doi:10.1029/WR020i003p00369, 1984.

Gouze, P. and Luquot, L.: X-ray microtomography characterization of porosity, permeability and reactive surface changes during dissolution, J. Contam. Hydrol., 120–121, 44–55, 2011.

Hamblin, W.: X-ray radiography in the study of structures in homogeneous sediments, J. Sediment. Petrol., 32, 133–145, 1962.

Hatiboglu, C. U. and Babadagli, T.: Experimental and visual analysis of diffusive mass transfer between matrix and fracture under static conditions, J. Petrol. Sci. Eng., 74, 31–40, doi:10.1016/j.petrol.2010.08.004, 2010.

Herm, D.: Paleontology, Naturwissenschaften, 63, 81–86, 1973.

Hinai, A. A., Rezaee, R., Esteban, L., and Labani, M.: Comparisons of pore size distribution: a case from the Western Australian gas shale formations, Journal of Unconventional Oil and Gas Resources, 8, 1–13, doi:10.1016/j.juogr.2014.06.002, 2014.

Hoshen, J. and Kopelman, R.: Percolation and cluster distribution. I. Cluster multiple labeling technique and critical concentration algorithm, Phys. Rev. B, 14, 3438–3445, doi:10.1103/PhysRevB.14.3438, 1976.

Ketcham, R. A. and Carlson, W. D.: Acquisition, optimization and interpretation of X-ray computed tomographic imagery: applications to the geosciences, Comput. Geosci., 27, 381–400, doi:10.1016/S0098-3004(00)00116-3, 2001.

Knackstedt, M. A., Arns, C. H., Saadatfar, M., Senden, T. J., Limaye, A., Sakellariou, A., Sheppard, A. P., Sok, R. M., Schrof, W., and Steininger, H.: Elastic and transport properties of cellular solids derived from three-dimensional tomographic images, P. Roy. Soc. Lond. A Mat., 462, 2833–2862, doi:10.1098/rspa.2006.1657, 2006.

Lamande, M., Wildenschild, D., Berisso, F. E., Garbout, A., Marsh, M., Moldrup, P., Keller, T., Hansen, S. B., de Jonge, L. W., and Schjonning, P.: X-ray CT and laboratory measurements on glacial till subsoil cores: assessment of inherent and compaction-affected soil structure characteristics, Soil Sci., 178, 359–368, doi:10.1097/SS.0b013e3182a79e1a, 2013.

Landry, C., Karpyn, Z., and Ayala, O.: Pore-scale lattice Boltzmann modeling and 4D X-ray computed microtomography imaging of fracture-matrix fluid transfer, Transport Porous Med., 103, 449–468, doi:10.1007/s11242-014-0311-x, 2014.

Lee, T.-C., Kashyap, R. L., and Chu, C.-N.: Building skeleton models via 3-D medial surface axis thinning algorithms, CVGIP-Graph. Model. Im., 56, 462–478, doi:10.1006/cgip.1994.1042, 1994.

Li, Y.-H. and Gregory, S.: Diffusion of ions in sea water and in deep-sea sediments, Geochim. Cosmochim. Ac., 38, 703–714, doi:10.1016/0016-7037(74)90145-8, 1974.

Louis, L., Wong, T.-F., and Baud, P.: Imaging strain localization by X-ray radiography and digital image correlation: deformation bands in Rothbach sandstone, J. Struct. Geol., 29, 129–140, doi:10.1016/j.jsg.2006.07.015, 2007.

Luquot, L. and Gouze, P.: Experimental determination of porosity and permeability changes induced by injection of CO_2 into carbonate rocks, Chem. Geol., 265, 148–159, 2009.

Luquot, L., Rodriguez, O., and Gouze, P.: Experimental characterization of porosity structure and transport property changes in limestone undergoing different dissolution regimes, Transport Porous Med., 101, 507–532, doi:10.1007/s11242-013-0257-4, 2014a.

Luquot, L., Roetting, T., and Carrera, J.: Characterization of flow parameters and evidence of pore clogging during limestone dissolution experiments, Water Resour. Res., 50, 6305, doi:10.1002/2013WR015193, 2014b.

Mangane, P. O., Gouze, P., and Luquot, L.: Permeability impairment of a limestone reservoir triggered by heterogeneous dissolution and particles migration during CO_2-rich injection, Geophys. Res. Lett., 40, 4614–4619, doi:10.1002/grl.50595, 2013.

Martys, N., Hagedorn, J., Goujon, D., and Devaney, J.: Large scale simulations of single and multi-component flow in porous media, SPIE, 3772, 309–403, 1999.

Mecke, K. R.: Additivity, convexity, and beyond: application of Minkovski functionals in statistical physics, Lect. Notes Phys., 554, 11–184, 2000.

Meijster, A., Roerdink, J. B., and Hesselink, W. H.: A general algorithm for computing distance transforms in linear time, in: Mathematical Morphology and its Applications to Image and Signal Processing, Springer Science+Business Media, New York, 331–340, 2002.

Menke, H. P., Bijeljic, B., Andrew, M. G., and Blunt, M. J.: Dynamic three-dimensional pore-scale imaging of reaction in a carbonate at reservoir conditions, Environ. Sci. Technol., 49, 4407–4414, doi:10.1021/es505789f, 2015.

Monna, F., Lancelot, J., Bernat, M., and Mercadier, H.: Sedimentation rate in the Thau Basin (France) according to geochronological, geochemical and stratigraphical data, Oceanol. Acta, 20, 627–638, 1997.

Nestle, N., Galvosas, P., Geier, O., Dakkouri, M., Zimmermann, C., and Kärger, J.: {NMR} studies of water diffusion and relaxation in hydrating slag-based construction materials, Magn. Reson. Imaging, 19, 547–548, doi:10.1016/S0730-725X(01)00301-0, 2001a.

Nestle, N., Zimmermann, C., Dakkouri, M., and Niessner, R.: Action and distribution of organic solvent contaminations in hydrating cement: time-resolved insights into solidification of organic waste, Environ. Sci. Technol., 35, 4953–4956, doi:10.1021/es015528y, 2001b.

Nimmo, J.: Porosity and pore size distribution, in: Encyclopedia of Soils in the Environment, edited by: Hillel, D., Elsevier, London, 295–303, 2004.

Noiriel, C., Luquot, L., Made, B., Raimbault, L., Gouze, P., and van der Lee, J.: Changes in reactive surface area during limestone dissolution: an experimental and modelling study, Chem. Geol., 265, 160–170, 2009.

Peng, S., Hu, Q., and Hamamoto, S.: Diffusivity of rocks: gas diffusion measurements and correlation to porosity and pore size distribution, Water Resour. Res., 48, w02507, doi:10.1029/2011WR011098, 2012.

Prodanovic, M., Bryant, S. L., and Karpyn, Z. T.: Investigating matrix/fracture transfer via a level set method for drainage and imbibition, SPE J., 15, 125–136, doi:10.2118/116110-PA, 2010.

Promentilla, M., Sugiyama, T., Hitomi, T., and Takeda, N.: Quantification of tortuosity in hardened cement pastes using synchrotron-based X-ray computed microtomography, Cement Concrete Res., 39, 548–557, doi:10.1016/j.cemconres.2009.03.005, 2009.

Reatto, A., da Silva, E., Bruand, A., Martins, E., and Lima, J.: Validata of the centrifuge method for determining the water retention properties of tropical soils, Soil Sci. Soc. Am. J., 72, 1547–1553, 2008.

Remeysen, K. and Swennen, R.: Application of microfocus computed tomography in carbonate reservoir characterization: possibilities and limitations, Mar. Petrol. Geol., 25, 486–499, doi:10.1016/j.marpetgeo.2007.07.008, 2008.

Roberts, A. P. and Garboczi, E. J.: Elastic properties of model porous ceramics, J. Am. Ceram. Soc., 83, 3041–3048, doi:10.1103/PhysRevE.54.2313, 2000.

Robinson, R. and Stokes, R. H.: Electrolyte Solutions: the Measurement and Interpretation of Conductance, Chemical Potential and Diffusion in Solutions of Simple Electrolytes, Academic press University of New England, New York, Butterworths, 1959.

Roetting, T. S., Luquot, L., Carrera, J., and Casalinuovo, D. J.: Changes in porosity, permeability, water retention curve and reactive surface area during carbonate rock dissolution, Chem. Geol., 403, 86–98, doi:10.1016/j.chemgeo.2015.03.008, 2015.

Schmidt, S., Jouanneau, J.-M., Weber, O., Lecroart, P., Radakovitch, O., Gilbert, F., and Jézéquel, D.: Sedimentary processes in the Thau Lagoon (France): from seasonal to century time scales, Estuar. Coast. Shelf S., 72, 534–542, doi:10.1016/j.ecss.2006.11.019, 2007.

Schwartz, L. M., Auzerais, F., Dunsmuir, J., Martys, N., Bentz, D. P., and Torquato, S.: Transport and diffusion in three-dimensional composite media, Physica A, 207, 28–36, 1994.

Sen, P. N.: Time-dependent diffusion coefficient as a probe of geometry, Concept. Magn. Reson. A, 23, 1–21, doi:10.1002/cmr.a.20017, 2004.

Siddiqi, K. and Pizer, S.: Medial Representations: Mathematics, Algorithms and Applications, 1st Edn., Springer Publishing Company, Incorporated, the Netherlands, 2008.

Smith, M. M., Sholokhova, Y., Hao, Y., and Carroll, S. A.: CO_2-induced dissolution of low permeability carbonates. Part I: Characterization and experiments, Adv. Water Resour., 62, 370–387, doi:10.1016/j.advwatres.2013.09.008, 2013.

Sturmer, W.: X-ray photography in paleontology-some new results, Naturwissenschaften, 60, 407–411, 1973.

Taina, I. A., Heck, R. J., and Elliot, T. R.: Application of X-ray computed tomography to soil science: a literature review, Can. J. Soil Sci., 88, 1–19, doi:10.4141/CJSS06027, 2008.

Torquato, S.: Random Heterogeneous Materials: Microstructure and Macroscopic Properties, Springer-Verlag, New York, 2002.

van Brakel, J. and Heertjes, P.: Analysis of diffusion in macroporous media in terms of a porosity, a tortuosity and a constrictivity factor, Int. J. Heat Mass Tran., 17, 1093–1103, doi:10.1016/0017-9310(74)90190-2, 1974.

Vogel, H.-J., Weller, U., and Schlüter, S.: Quantification of soil structure based on Minkowski functions, Comput. Geosci., 36, 1236–1245, doi:10.1016/j.cageo.2010.03.007, 2010.

Wildenschild, D. and Sheppard, A. P.: X-ray imaging and analysis techniques for quantifying pore-scale structure and processes in subsurface porous medium systems, Adv. Water Resour., 51, 217–246, doi:10.1016/j.advwatres.2012.07.018, 2013.